nature nanotechnology

LETTERS

PUBLISHED ONLINE: 21 OCTOBER 2012 | DOI: 10.1038/NNANO.2012.176

Photoresponse of a strongly correlated material determined by scanning photocurrent microscopy

T. Serkan Kasırga[1], Dong Sun[1], Jae H. Park[1], Jim M. Coy[1], Zaiyao Fei[1], Xiaodong Xu[1,2]* and David H. Cobden[1]*

The generation of a current by light is a key process in optoelectronic and photovoltaic devices. In band semiconductors, depletion fields associated with interfaces separate long-lived photo-induced carriers. However, in systems with strong electron–electron and electron–phonon correlations it is unclear what physics will dominate the photoresponse. Here, we investigate photocurrent in VO_2, an exemplary strongly correlated material known for its dramatic metal–insulator transition[1–3] at $T_c \approx 68$ °C, which could be useful for optoelectronic detection and switching up to ultraviolet wavelengths[4–10]. Using scanning photocurrent microscopy on individual suspended VO_2 nanobeams we observe a photoresponse peaked at the metal–insulator boundary but extending throughout both insulating and metallic phases. We determine that the response is photothermal, implying efficient carrier relaxation to a local equilibrium in a manner consistent with strong correlations[11–14]. Temperature-dependent measurements reveal subtle phase changes within the insulating state. We further demonstrate switching of the photocurrent by optical control of the metal–insulator boundary arrangement. Our work shows the value of applying scanning photocurrent microscopy to nanoscale crystals in the investigation of strongly correlated materials, and the results are relevant for designing and controlling optoelectronic devices employing such materials.

Strongly correlated materials offer potential for applications beyond the limits of semiconductor technologies, but their complex nature makes it challenging to determine the fundamental mechanisms behind their behaviour. In the case of VO_2, recent progress[15–27] in working with crystals smaller than the characteristic domain size has allowed clarification of a number of aspects that were obscured by domain structure and other crystal imperfections in earlier bulk studies. These include improved measurements of the resistivity[18–20], activation energy and optical gap in the insulator[26], establishing the existence of a threshold resistivity for the transition[18,20], and an improved understanding of the interplay between the two similar monoclinic insulating (I) phases, M1 and M2 (for structures see Fig. 1), alongside the rutile metallic (M) phase near the metal–insulator transition (MIT)[20–25]. The resulting improved level of control and understanding of VO_2 now presents the opportunity to investigate methodically the optoelectronic response of a strongly correlated electronic material.

We applied scanning photocurrent microscopy (SPCM; see Methods) at a wavelength of 800 nm (1.55 eV, well above the 0.6 eV optical gap in the insulator) to suspended VO_2 nanobeam devices (Fig. 1). Suspending the nanobeams removes complications arising from non-uniform stress caused by substrate adhesion[17,18], but an axial stress is still present as a result of the firm attachment under the contacts. Figure 2 shows measurements at a low laser

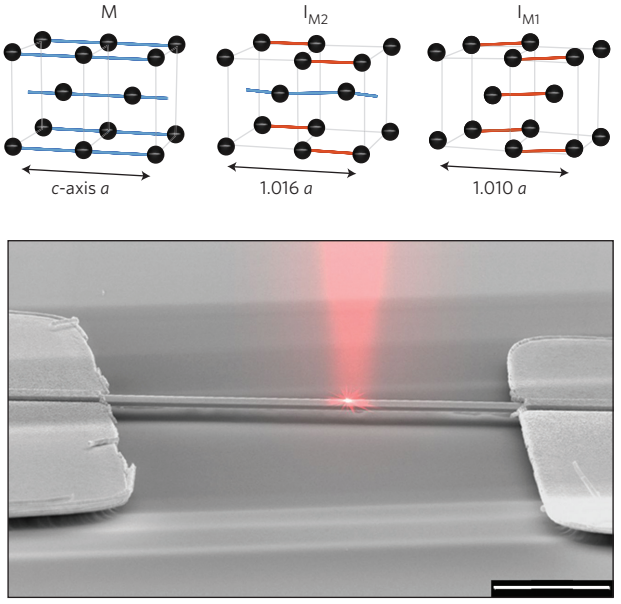

Figure 1 | SPCM on a suspended VO_2 nanobeam device. A focused laser is depicted superimposed on a scanning electron microscopy (SEM) image of a VO_2 nanobeam suspended between gold electrical contacts. Top: sketches of the arrangement of vanadium atoms in the tetragonal metallic phase (M) and monoclinic insulating phases (I_{M1} and I_{M2}). Grey lines indicate two tetragonal unit cells (oxygen atoms are not shown). The M phase is shortest along the tetragonal *c*-axis, which is the nanobeam axis, and has only periodic vanadium chains (blue lines). I_{M2} is longest and has half the vanadium atoms dimerized (red lines). I_{M1} has intermediate length and all vanadium atoms dimerized. Scale bar, 5 μm.

power of $P = 1.0$ μW ($\sim$20 W cm^{-2}) for two similar nanobeams. Figure 2a–c presents greyscale plots of reflected intensity versus laser position. Device 1, at 30 °C, is well below T_c and is uniformly in the M1 insulating (I_{M1}) phase, as determined by Raman spectroscopy and resistivity measurements (Supplementary Information). Device 2, at 75 °C and 95 °C, is above T_c and shows a darker metallic (M) region in coexistence with a paler insulating region. The latter is in the M2 phase (I_{M2}), because the axial tension stabilizes the insulating phase with the longer *c*-axis lattice constant[28] (Fig. 1). We oriented the devices with the insulating region on the left, with bias V applied to the left contact and photocurrent I_{ph} measured out of the right contact. In the second row of Fig. 2 are corresponding colourscale maps of the zero-bias photocurrent I_0. Below T_c (Fig. 2d), I_0 is very small, but above T_c (Fig. 2e,f) it is much larger, positive, and extends along the entire nanobeam,

[1]Department of Physics, University of Washington, Seattle, Washington 98195, USA, [2]Department of Materials Science and Engineering, University of Washington, Seattle, Washington 98195, USA. *e-mail: xuxd@uw.edu; cobden@uw.edu

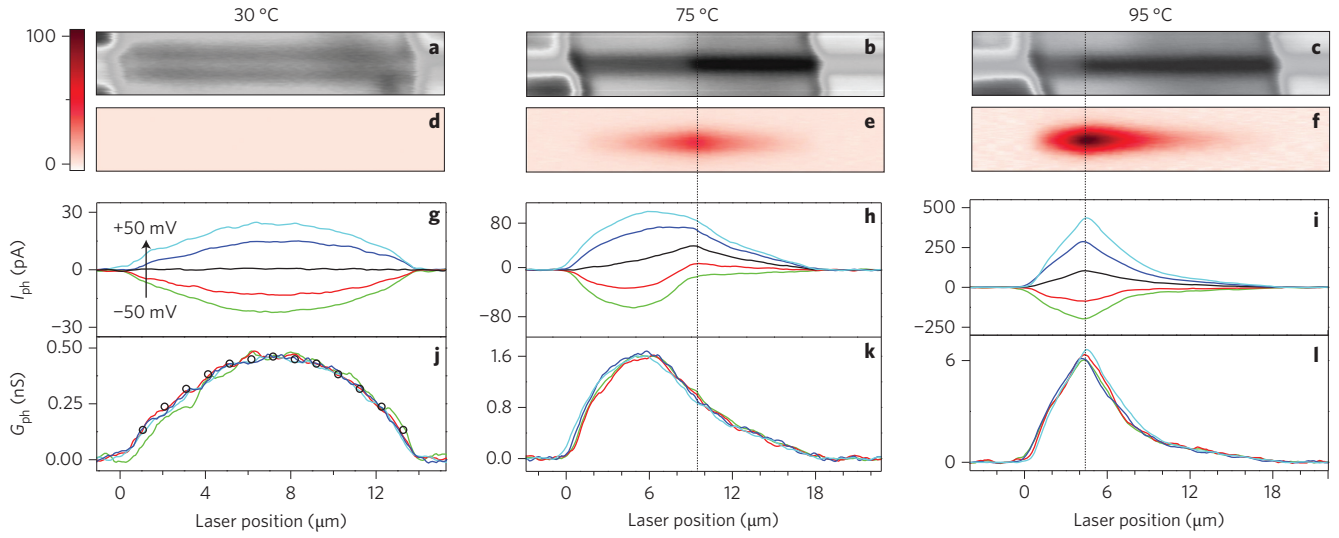

Figure 2 | Photocurrent measurements at temperatures across the MIT. Data at 30 °C (left column) are from one nanobeam (device 1). Those at 75 °C and 95 °C (centre and right columns) are from another very similar nanobeam (device 2). The laser power is $P = 1.0$ μW. **a–c**, Reflected light images. The metallic phase appears darker. **d–f**, Corresponding zero-bias photocurrent images. **g–i**, Photocurrent I_{ph} along the centreline of the nanobeam for voltage biases $V = -50$, -30, 0 (I_0, in black), 30 and 50 mV. **j–l**, Photoconductance $G_{ph} = (I_{ph} - I_0)/V$, which can be seen to be independent of V. Circles in **j** plot the function $G_0 x_l(1-x_l)$ predicted for a thermal resistance change (see text), where x_l is fractional position along the nanobeam and fitting parameter $G_0 = 1.9$ nS.

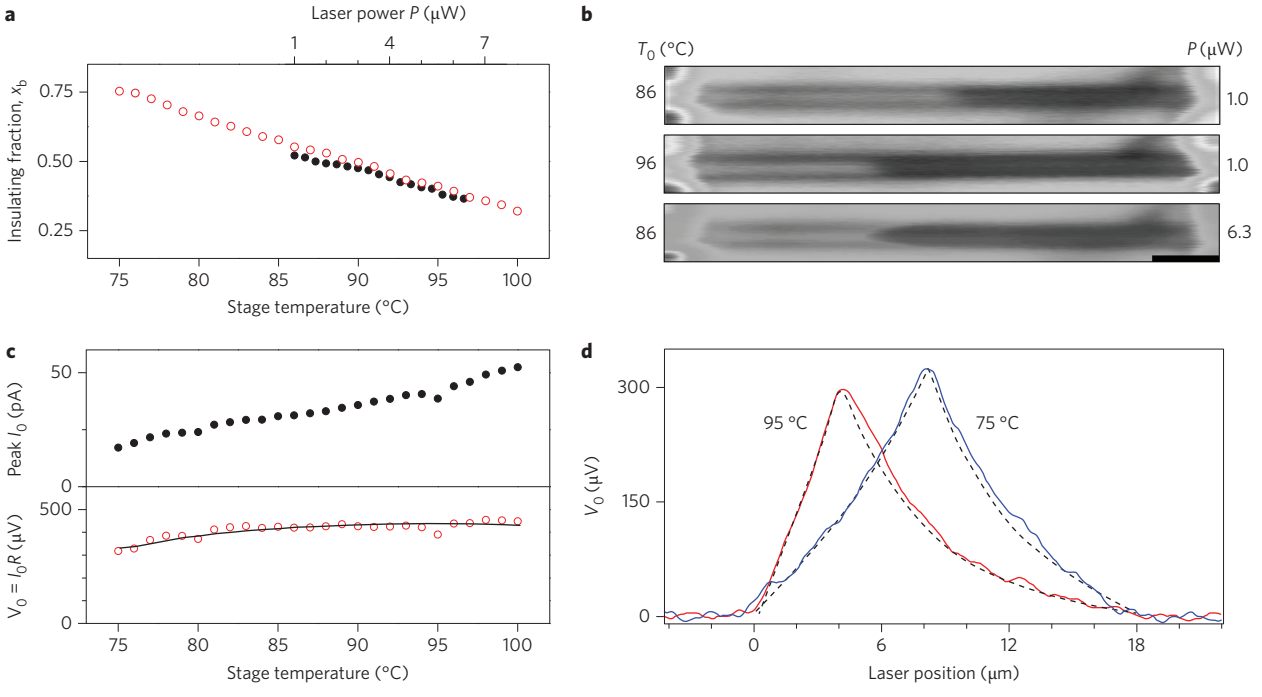

Figure 3 | Evidence for the thermoelectric origin of the photocurrent. a, Comparison of the variation of insulating fraction x_b with stage temperature T_0 for device 1 at a laser power of $P = 1.0$ μW (red open circles), and with P at $T_0 = 86$ °C (black filled circles). **b**, Reflection images (generated by the scanning laser spot) illustrating the comparison. Scale bar, 2 μm. **c**, Temperature dependence of the peak zero-bias photocurrent I_0 (upper panel, black filled circles) and emf $V_0 = I_0R$ (lower panel, red open circles) for device 1. **d**, Variation of V_0 with laser position for device 2 at 75 °C and 95 °C. The solid line in **c** and dashed lines in **d** are the predicted photothermal emf (see text).

reaching a maximum at the I–M boundary. Figure 2g–i shows the variation of I_0 along the centreline of the nanobeam (thick black line), together with the variation of I_{ph} measured at several finite biases. The change in current due to the bias can be described entirely in terms of a bias-independent photoconductance $G_{ph} = (I_{ph}-I_0)/V$, as shown in Fig. 2j–l.

To understand these measurements, we began by exploiting the phase transition itself to quantify the rise in temperature under the laser spot by observing the position of the I–M boundary[18] above T_c. The fraction x_b of insulator (I_{M2}) in the nanobeam depends on the lattice temperature T_b at the boundary, because x_b determines the axial tension, which must be appropriate for the

two phases to coexist at T_b. x_b decreases with increasing stage temperature T_0, as shown by the red circles in Fig. 3a. It also decreases with increasing laser power P at fixed T_0, as shown by the black circles. By comparing the effects of increasing P and T_0, as illustrated in Fig. 3b, we deduce that for device 1 the local temperature rise of the lattice with the laser near the middle is ~1.5 °C per μW of laser power.

At higher P the interface has a curved appearance (Fig. 3b, bottom image). This is because the power absorbed is greatest when the laser is focused on the centreline of the nanobeam, so the temperature rise and boundary shift are also greater. In fact, as P increases, the arrangement of the phases is increasingly disturbed by the laser, and when $P > \sim 10$ μW the metallic region is dragged along by the laser beam, leading to complex nonlinear behaviour. We therefore confine our studies to lower power levels where the response is linear in P.

Using this knowledge of the temperature rise we next considered the photoconductance. Well below T_c, when the nanobeam is entirely in the I_{M1} phase (Fig. 2j), the negative temperature coefficient of the insulator resistivity $\rho_I(T)$ will lead to a conductance increase ΔG under illumination. For a small temperature rise $\delta T(x)$, where coordinate x runs from 0 at the left contact to 1 at the right, $\Delta G \approx -(1/R^2)(dR/dT)\delta T_{av}$, where $\delta T_{av} = \int_0^1 \delta T(x)\,dx$, and $R(T)$ is the resistance of the nanobeam held at uniform temperature T (see Supplementary Information for details). If we assume that all the heat flows along the nanobeam, then $\delta T(x)$ drops linearly to zero at the gold contacts and $\delta T_{av} = \delta T(x_l)/2 \propto x_l(1-x_l)$, where x_l is the laser position. For the laser at 1.0 μW in the middle, we know from above that $\delta T(x_l = 1/2) \approx 1.5$ °C, and using the independently measured dark resistance $R = 42$ MΩ and $dR/dT = 1.4$ MΩ °C^{-1} we obtain $\Delta G \approx 0.6$ nS. The measured photoconductance $G_{ph} = 0.5$ nS at $x_l = 1/2$ is slightly smaller than this, which is explained by heat loss through the air making δT_{av} smaller than $\delta T(x_l)/2$ (see below). In addition, the predicted variation with laser position, $\Delta G \propto x_l(1-x_l)$, is an excellent match to the experimentally determined G_{ph}, as shown by the open circles in Fig. 2j.

Above T_c, when an I–M boundary is present (Fig. 2k,l), the decrease in the insulating fraction x_b with boundary temperature rise $\delta T_b \equiv T_b - T_0$ results in a conductance increase that is largest when δT_b is maximum, that is, when $x_l = x_b$ (Supplementary Information). This explains the fact that G_{ph} peaks at the boundary at 95 °C. More complex behaviour results when the effect of the change in $\rho_I(T)$ is comparable, as is the case at 75 °C. In summary, both above and below T_c the measured photoconductance can be well understood as the result of the temperature rise of the lattice, with no hint of any other contribution.

We are now in a position to analyse the zero-bias photocurrent I_0 seen above T_c (Fig. 2e,f). If carrier relaxation to complete equilibrium with the lattice is fast, then I_0 will be purely photothermal (thermoelectric), so we consider this possibility first. The lattice temperature difference (δT_b) between the I–M boundary and the gold contacts will generate a thermoelectric electromotive force (emf), $V_{te} = -\Delta S_{IM}\delta T_b$, due to the difference in Seebeck coefficients, $\Delta S_{IM} = S_I - S_M$, between the I_{M2} and M phases. From the literature[27,29], $S_I \approx -350$ μV °C^{-1} (for I_{M2}) and $S_M \approx -20$ μV °C^{-1}, so $\Delta S_{IM} \approx -330$ μV °C^{-1}. Hence, when the laser at 1 μW is focused near the middle, giving $\delta T_b \approx 1.5$ °C for device 1, as found above, we expect $V_{te} \approx +500$ μV. Figure 3c shows the temperature dependence of the peak value of I_0 and the corresponding emf, $V_0 = I_0 R$. V_0 reaches ~+ 450 μV, in excellent agreement with V_{te} considering the uncertainty in knowledge of the thermoelectric coefficients.

Moreover, we can calculate the variation of V_{te} with laser position, allowing for different thermal conductivities κ_M and $\kappa_{I_{M2}}$ of the two phases and for heat loss $\beta\delta T$ through the air (Supplementary Section S4). Figure 3d shows the measured variation

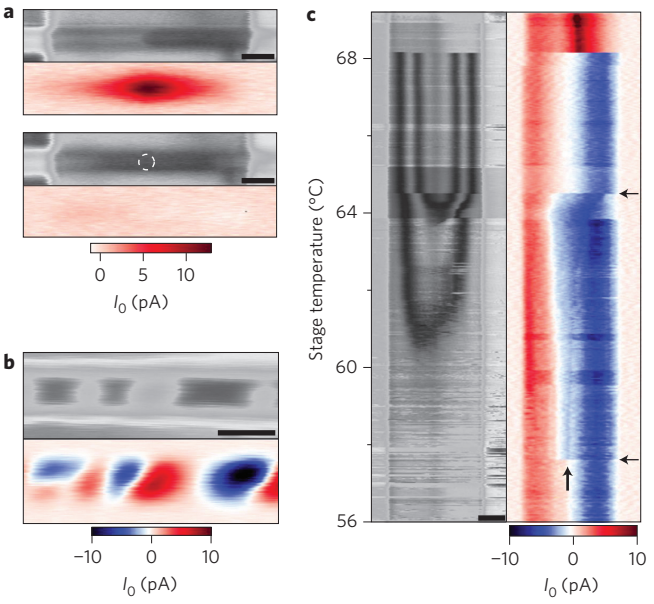

Figure 4 | Optical control of the photocurrent and imaging the evolution of the insulating phase. a, Reflection and zero-bias photocurrent images of device 1 at 70 °C and with $P = 1.0$ μW, without (above) and with (below) a second laser ($P = 2.4$ μW) focused at the location of the dashed circle. **b**, Similar images of an unsuspended nanobeam ($P = 0.6$ μW). **c**, Reflection (left) and photocurrent (right) measured by repeatedly scanning along the centreline of a nanobeam (device 3) while ramping the temperature up to and beyond the transition at 68.2 °C. Horizontal black arrows indicate where the conversion of I_{M1} to I_{M2} begins (lower) and completes (upper). Scale bars, 2 μm (**a**,**b**) and 5 μm (**c**).

of V_0 with laser position (solid lines) for device 2 at 75 °C and 95 °C, compared with results for the calculation of V_{te} (dashed lines). Here, we used[30] $\kappa_I = 3.5$ W m^{-1} °C^{-1} and $\kappa_M/\kappa_I = 2$, and treated β and the fraction γ of the laser power absorbed as fitting parameters, yielding $\beta = 0.03$ W °C^{-1} m^{-1}, consistent with the thermal conductivity of air, and $\gamma = 0.5$. We also calculated the temperature variation of the peak value of V_{te}, which occurs for the laser at the I–M boundary ($x_l = x_b$), again obtaining excellent agreement with the temperature dependence of V_0 (see the solid line in Fig. 3c; for this device $\gamma = 0.6$). We conclude that the dominant photocurrent contribution follows directly from the rise in lattice temperature, just as does the photoconductance.

Having established that the photocurrent is predominantly photothermal, we now address the question of whether there is any additional contribution from the separation of non-equilibrium carriers that diffuse to the I/M interface, as might be expected in a band semiconductor like silicon[31,32]. Such a contribution is not possible for excitation in the metallic phase, because electron-lattice relaxation occurs in picoseconds in all metals (there being no gap to block low-energy processes). Accordingly, the photocurrent signal seen extending many micrometres into the metallic region (Fig. 2h) must be entirely photothermal. As the photothermal mechanism consistently explains the entire observed photocurrent equally well in both metallic and insulating parts, we deduce that any additional contribution in the insulator is insignificant. This is consistent with efficient local carrier relaxation in insulating VO_2, which keeps the material very close to local thermal equilibrium during illumination. Evidence for fast relaxation is provided by the fact that the photocurrent we measure is identical for pulsed (0.25 ps pulses repeated at 76 MHz) and for continuous-wave excitation at the same average power. In addition, we saw exactly the same behaviour using different laser wavelengths, consistent

with only the absorbed power being relevant (Supplementary Information). We note that there are no reports of non-equilibrium carrier effects such as luminescence in the optical response of insulating VO_2 in the literature. Moreover, the strong electron–phonon coupling and polaronic effects, which are likely in such a material, provide a natural mechanism for efficient relaxation through interband scattering and slow diffusion. This is congruent with the very short scattering length, roughly equal to the lattice constant, that can be inferred from the poor conductivity of the metallic phase and the prefactor of the activated insulator conductivity.

The photothermal origin of the photocurrent is further supported by a number of other observations. First, if the metallic region is pulled into the centre of the nanobeam using a second identical fixed laser spot, resulting in two opposing I–M boundaries, then I_0 almost vanishes for all positions of the scanning laser (Fig. 4a). This follows from the fact that the temperatures at both boundaries must be the same for the two phases to coexist under the same axial strain. Hence, the boundaries generate emfs of equal magnitude but opposite sign and the sum vanishes. Such a vanishing of the photoresponse, independent of laser position, would not occur for other mechanisms. Second, for a nanobeam not released from the substrate by etching, multiple alternating I and M domains occur due to inhomogeneous strain[17], and we see associated peaks in I_0 of alternating sign centred at the I–M boundaries (Fig. 4b). This is explained by the fact that in this case thermal conduction through the substrate causes the temperature rise to be much more localized to the laser spot, so the thermoelectric emf is large only when the laser is close to an I–M boundary.

Finally, we illustrate how SPCM can be exploited to study such a solid-state phase transition by allowing the visualization of interphase boundaries that are otherwise invisible. For example, interconversion between I_{M1} and I_{M2} near the MIT[21–25] may be revealed even though the two phases are optically almost indistinguishable. Figure 4c shows the reflection signal (left) and zero-bias photocurrent (right) measured while repeatedly scanning along the centreline of a nanobeam as the temperature is ramped up. Above 68.2 °C, the nanobeam is straight and in I_{M2}–M coexistence, and I_0 peaks at the boundary. Below 57.5 °C it is straight and fully I_{M1}. As the temperature rises from 57.5 °C to 64.5 °C (between the two horizontal arrows), a stripe pattern develops in the reflection signal because the nanobeam gradually becomes buckled due to conversion from I_{M1} to I_{M2}, with its longer *c*-axis. During this process a feature appears in the photocurrent near the middle of the nanobeam (open arrow) and steadily expands. The feature may reflect an I_{M2} domain nucleating and growing, made visible by the difference in photoresponse between I_{M2} and I_{M1}.

In summary, we have determined the relationship between the optical and direct-current electrical properties of VO_2 using SPCM, which probes the optoelectronic properties of the phases and their interfaces. We observe photoconductance and zero-bias photocurrent generation that is entirely of photothermal origin, consistent with very efficient electron-lattice relaxation in the strongly correlated insulating phase and in stark contrast to the response of uncorrelated band insulators.

Methods

To perform SPCM, a diffraction-limited 800 nm laser spot, chopped at 1 kHz, was scanned over the sample on a heated stage, in air, and the resulting photocurrent was measured with a current preamplifier and a lock-in amplifier referenced to the chopper. The reflected laser light was detected by a silicon photodiode, generating an image of the device corresponding directly to the photocurrent image. The nanobeams were grown by physical vapour transport[16] using a V_2O_5 source placed in an alumina crucible in the centre of a tube furnace at ~900 °C and with argon carrier gas at a few mbar. The substrate was a p-doped (100) silicon chip with a 2 μm wet oxide coating. The nanobeams grew elongated along the tetragonal *c*-axis with {110} sides[16]. The contacts (10 nm titanium followed by 200 nm gold) were made by photolithography followed by electron-beam evaporation and liftoff, and the nanobeams were suspended by immersing the devices in buffered oxide etch for several minutes.

Received 19 June 2012; accepted 13 September 2012; published online 21 October 2012

References

1. Morin, F. J. Oxides which show a metal-to-insulator transition at the Neel temperature. *Phys. Rev. Lett.* **3,** 34–36 (1959).
2. Zylbersztejn, A. & Mott, N. F. Metal–insulator transition in vanadium dioxide. *Phys. Rev. B* **11,** 4383–4395 (1975).
3. Eyert, V. The metal–insulator transitions of VO_2: a band theoretical approach. *Ann. Phys. Berlin* **11,** 650–702 (2002).
4. Verleur, H. W., Barker, A. S. & Berglund, C. N. Optical properties of VO_2 between 0.25 and 5 eV. *Phys. Rev.* **172,** 788–798 (1968).
5. Driscoll, T. *et al.* Dynamic tuning of an infrared hybrid-metamaterial resonance using vanadium dioxide. *Appl. Phys. Lett.* **93,** 024101 (2008).
6. Becker, M. F., Buckman, A. B. & Walser, R. M. Femtosecond laser excitation of the semiconductor–metal phase transition in VO_2. *Appl. Phys. Lett.* **65,** 1507–1509 (1994).
7. Rini, M. *et al.* Optical switching in VO_2 films by below-gap excitation. *Appl. Phys. Lett.* **92,** 181904 (2008).
8. Cavalleri, A., Rini, M. & Schoenlein, R. W. Ultra-broadband femtosecond measurements of the photo-induced phase transition in VO_2: from the mid-IR to the hard X-rays. *J. Phys. Soc. Jpn* **75,** 011004 (2006).
9. Hilton, D. J. *et al.* Enhanced photosusceptibility near T_c for the light-induced insulator-to-metal phase transition in vanadium dioxide. *Phys. Rev. Lett.* **99,** 226401 (2007).
10. Kubler, C. *et al.* Coherent structural dynamics and electronic correlations during an ultrafast insulator-to-metal phase transition in VO_2. *Phys. Rev. Lett.* **99,** 116401 (2007).
11. Wentzcovitch, R. M., Schulz, W. W. & Allen, P. B. VO_2: Peierls or Mott–Hubbard? A view from band theory. *Phys. Rev. Lett.* **72,** 3389–3392 (1994).
12. Rice, T. M., Launois, H. & Pouget, J. P. Comment on 'VO_2: Peierls or Mott–Hubbard? A view from band theory'. *Phys. Rev. Lett.* **73,** 3042 (1994).
13. Kim, H. T. *et al.* Monoclinic and correlated metal phase in VO_2 as evidence of the Mott transition: coherent phonon analysis. *Phys. Rev. Lett.* **97,** 266401 (2006).
14. Kim, B-J. *et al.* Micrometer X-ray diffraction study of VO_2 films: separation between metal–insulator transition and structural phase transition. *Phys. Rev. B* **77,** 235401 (2008).
15. Lopez, R., Feldman, L. C. & Haglund, R. F. Jr Size-dependent optical properties of VO_2 nanoparticle arrays. *Phys. Rev. Lett.* **93,** 177403 (2004).
16. Guiton, B. S., Gu, Q., Prieto, A. L., Gudiksen, M. S. & Park, H. Single-crystalline vanadium dioxide nanowires with rectangular cross sections. *J. Am. Chem. Soc.* **127,** 498–499 (2005).
17. Wu, J. Q. *et al.* Strain-induced self organization of metal–insulator domains in single-crystalline VO_2 nanobeams. *Nano Lett.* **6,** 2313–2317 (2006).
18. Wei, J., Wang, Z. H., Chen, W. & Cobden, D. H. New aspects of the metal–insulator transition in single-domain vanadium dioxide nanobeams. *Nature Nanotech.* **4,** 420–424 (2009).
19. Cao, J. *et al.* Strain engineering and one-dimensional organization of metal–insulator domains in single-crystal vanadium dioxide beams. *Nature Nanotech.* **4,** 732–737 (2009).
20. Cao, J. *et al.* Constant threshold resistivity in the metal–insulator transition of VO_2. *Phys. Rev. B* **82,** 241101 (2010).
21. Cao, J. *et al.* Extended mapping and exploration of the vanadium dioxide stress–temperature phase diagram. *Nano Lett.* **10,** 2667–2673 (2010).
22. Zhang, S. X., Chou, J. Y. & Lauhon, L. J. Direct correlation of structural domain formation with the metal insulator transition in a VO_2 nanobeam. *Nano Lett.* **9,** 4527–4532 (2009).
23. Tselev, A. *et al.* Symmetry relationship and strain-induced transitions between insulating M1 and M2 and metallic R phases of vanadium dioxide. *Nano Lett.* **10,** 4409–4416 (2010).
24. Sohn, J. I. *et al.* Surface-stress-induced Mott transition and nature of associated spatial phase transition in single crystalline VO_2 nanowires. *Nano Lett.* **9,** 3392–3397 (2009).
25. Jones, A. C., Berweger, S., Wei, J., Cobden, D. & Raschke, M. B. Nano-optical investigations of the metal–insulator phase behavior of individual VO_2 microcrystals. *Nano Lett.* **10,** 1574–1581 (2010).
26. Liu, W. T. *et al.* Intrinsic optical properties of vanadium dioxide near the insulator–metal transition. *Nano Lett.* **11,** 466–470 (2011).
27. Cao, J., Fan, W., Zheng, H. & Wu, J. Thermoelectric effect across the metal–insulator domain walls in VO_2 microbeams. *Nano Lett.* **9,** 4001–4006 (2009).
28. Marezio, M., McWhan, B., Dernier, P. D. & Remeika, J. P. Structural aspects of metal–insulator transitions in Cr-doped VO_2. *Phys. Rev. B* **5,** 2541–2551 (1972).
29. Berglund, C. N. & Guggenheim, H. J. Electronic properties of VO_2 near the semiconductor–metal transition. *Phys. Rev.* **185,** 1022–1033 (1969).

30. Oh, D. W., Ko, C., Ramanathan, S. & Cahill, D. G. Thermal conductivity and dynamic heat capacity across the metal–insulator transition in thin film VO_2. *Appl. Phys. Lett.* **96,** 151906 (2010).
31. Graham, R., Miller, C., Triplett, M. & Yu, D. Scanning photocurrent microscopy in single nanowire devices. *Proc. SPIE* **8106,** 81060–81061 (2011).
32. Miller, C. *et al.* Unusually long free carrier lifetime and metal–insulator band offset in vanadium dioxide. *Phys. Rev. B* **85,** 085111 (2012).

Acknowledgements

This work was supported by the US Department of Energy, Office of Basic Energy Sciences, Division of Materials Sciences and Engineering (award DE-SC0002197), by the Army Research Office (contract 48385-PH) and by an NSF Career Award (DMR-1150719, to X.X.). The authors thank B. Spivak for helpful discussions.

Author contributions

All authors participated in the experiments, discussed the results, commented on the manuscript, and made critical contributions to the work.

Additional information

Supplementary information is available in the online version of the paper. Reprints and permission information is available online at http://www.nature.com/reprints. Correspondence and requests for materials should be addressed to X.X. and D.H.C.

Competing financial interests

The authors declare no competing financial interests.